Revision 2 Word count: 9592

The occurrence of monoclinic jarosite in natural environments

Anne J. Whitworth[1]*, Helen E. A. Brand[2], Siobhan A. Wilson[3], Ian E. Grey[4], Natasha R. Stephen[5], Yesim Gozukara[6], Andrew J. Frierdich[1]

[1] Monash Isotopia Laboratory, School of Earth, Atmosphere & Environment, Monash University, Clayton, Victoria, Australia

[2] Australian Synchrotron, Clayton, Victoria, Australia

[3] Department of Earth and Atmospheric Sciences, University of Alberta, Edmonton, Alberta T6G 2E3, Canada

[4] CSIRO Mineral Resources, Private Bag 10, Clayton South, Victoria 3169, Australia

[5] Plymouth Electron Microscopy Centre, University of Plymouth, Drake Circus, Plymouth PL4 8AA, UK

[6] CSIRO Manufacturing, Private Bag 10, Clayton South, Victoria 3169, Australia

Submitted to American Mineralogist

August 2021

*Corresponding author at: E-mail: anne.whitworth@earthsystems.com.au

Footnote: Anne J Whitworth presently at Earth Systems, Victoria, Australia

This is the peer-reviewed, final accepted version for American Mineralogist, published by the Mineralogical Society of America.
The published version is subject to change. Cite as Authors (Year) Title. American Mineralogist, in press.
DOI: https://doi.org/10.2138/am-2022-8276. http://www.minsocam.org/

ABSTRACT

Jarosite and related subgroup minerals are of high importance in mineral processing, as sources and sinks for metals and acidity in the environment, and they have potential to preserve elemental and isotopic biomarkers relevant to the search for life in the solar system. The crystal structures and chemistry of jarosite minerals affect their stability and reactivity and thus the roles they play in natural and engineered systems. Rhombohedral symmetry has been documented in natural and synthetic jarosites, whereas monoclinic symmetry has only been documented in synthetic jarosites. This research reports the occurrence of monoclinic symmetry in a natural natrojarosite sample investigated using synchrotron powder X-ray diffraction (PXRD), thermogravimetric analysis (TGA), and electron backscatter diffraction (EBSD). Splitting of several rhombohedral PXRD peaks (e.g., 012, 027 and 033) into pairs of peaks was observed, with the magnitude of the splitting and the relative intensities of the pairs of peaks being almost identical to those reported for synthetic monoclinic jarosite. Rietveld refinement with room temperature PXRD data shows an ordering of iron-site vacancies on the Fe1 site consistent with monoclinic symmetry, space group C2/*m*. Conversion of monoclinic unit-cell parameters into pseudohexagonal unit-cell parameters, specifically β′, also supports the use of a monoclinic model to describe the natrojarosite structure. Structural analysis with increasing temperature is supportive of the thermal evolution previously described for synthetic monoclinic jarosite samples, with some indications of subtle differences between synthetic and natural materials including slower rates of thermal expansion and absence of $FeOHSO_4$ peaks for natural monoclinic jarosite. EBSD provides insight into the spatial–structural variation within the hand specimen from which the natrojarosite was sampled, demonstrating that there are areas of unambiguous monoclinic symmetry, but others where both monoclinic and rhombohedral

natrojarosite coexist. The results of this study suggest that monoclinic symmetry in natural jarosites may be more prevalent than previous studies suggest. Monoclinic symmetry in jarosites is identifiable by an ordering of iron-site vacancies on the Fe1 site, splitting of specific rhombohedral XRD peaks into pairs of peaks, and an increase in jarosite symmetry (i.e., from monoclinic to rhombohedral) during heating. The splitting of peaks in monoclinic jarosites can be subtle so it is recommended that high-resolution XRD data is collected when studying the crystal structure of jarosites.

Keywords: Jarosite, natrojarosite, monoclinic symmetry, synchrotron powder X-ray diffraction, Rietveld refinement, electron backscatter diffraction

INTRODUCTION

Jarosite [$KFe_3(SO_4)_2(OH)_6$] and related subgroup minerals are of high importance in a variety of mineral processing and natural environments. Jarosite has been documented in acid-sulfate environments such as acid mine drainage and acid sulfate soils (e.g., Egal et al., 2008; Jamieson et al., 2005; Öborn and Berggren, 1995; Welch et al., 2007) where it can act as a contaminant sink, incorporating toxic metal(loids) into its structure (Asta et al., 2009; Johnston et al., 2010), or as a contaminant source through release of acid and toxic metal(oid)s during its decomposition (Karimian et al., 2017; Langmuir, 1997; Smith et al., 2006a). In some mineral processing industries (e.g., zinc), jarosite is deliberately precipitated to remove unwanted iron, a procedure known as the 'jarosite process' (Arregui et al., 1980), and maximization of iron incorporation during jarosite precipitation is essential. In other mineral processing technologies (e.g., bioleaching of chalcopyrite), jarosite precipitation forms unwanted passivating layers on

ore minerals, slowing mineral dissolution and metal recovery (Sandström et al., 2005; Stott et al., 2000). Knowledge of jarosite formation mechanisms, stability and thermal behavior is therefore essential for its management and utilization in the environment and during mineral processing. Jarosite has also been documented at several locations on Mars including Meridiani Planum, Melas Chasma and Mt Sharp (e.g., Klingelhöfer et al., 2004; Liu et al., 2018; Rampe et al., 2017, 2020), sparking interest in its potential to shed light on geological processes acting on Mars in the past. Jarosite is also of theoretical interest as a model compound for spin frustration in Kagomè-Heisenberg antiferromagnetic materials (Grohol et al., 2003; Nishiyama et al., 2003; Wills et al., 2000).

The jarosite subgroup forms a subset of the alunite supergroup, which has the general formula $DG_3(TO_4)_2(OH)_6$ (Bayliss et al., 2010), with the jarosite subgroup being characterized by the predominance of Fe^{3+} and S^{6+} in the G and T sites, respectively. In nature, Na frequently substitutes for K in the D site of jarosite, forming natrojarosite [$NaFe_3(SO_4)_2(OH)_6$] (Desborough et al., 2010; Stoffregen et al., 2000; Whitworth et al., 2020). End-member compositions seldom occur in nature; most jarosite subgroup minerals typically are a solid solution due to substitution of different ions into the D, G and T sites (e.g., Stoffregen et al., 2000; Whitworth et al., 2020). Substitution of different ions into the D, G and T sites affects the structure of jarosite (Stoffregen et al., 2000), and structural changes due to ion substitution and other processes (e.g., heating) have been found to cause changes to the volume, heat capacity, stability and reactivity of jarosite subgroup minerals (e.g., Brand et al., 2017; Grey et al., 2013; Majzlan et al., 2010; Welch et al., 2007), with implications for jarosite behavior in the environment and mineral processing. The jarosite samples investigated here have been determined to be sodium-rich and thus can be classified as natrojarosites.

Most natural and synthetic jarosites crystallize in the rhombohedral space group $R\bar{3}m$, with unit-cell parameters of a_h ~7.3 Å and c_h ~17 Å. The jarosite structure consists of a trigonal network of sulfate tetrahedra and chains of corner-sharing Fe-centered octahedra that form kagomè layers perpendicular to the *c* axis (Figure 1A; Basciano and Peterson, 2008; Grey et al., 2013). Substitution of typically monovalent ions into the larger D site mainly affects the dimension of the *c* axis whereas substitutions in the smaller G site mainly affect the *a* axis (Stoffregen et al., 2000). During synthesis, the formation of stoichiometric rhombohedral jarosites is favored at high (≥140 °C) temperatures and in Fe-rich fluids (Basciano and Peterson, 2007; Basciano and Peterson, 2008; Dutrizac, 1983) whereas the formation of non-stoichiometric rhombohedral jarosites is favored in dilute solutions at typically lower (~100 °C or less) temperatures (Drouet and Navrotsky, 2003; Kubisz, 1970; Savage et al., 2005). Non-stoichiometric rhombohedral jarosite has been observed to transform to stoichiometric jarosite at 170 °C due to dehydration and exsolution of butlerite-like regions to form $FeOHSO_4$ (Grey et al., 2013).

Monoclinic symmetry *C*2/*m*, has only been reported for synthetic jarosites (Brand et al., 2012; Gottlicher et al., 2000; Grey et al., 2011; Grey et al., 2013; Scarlett et al., 2013; Scarlett et al., 2010). The monoclinic jarosite structure reflects ordering of iron-site vacancies onto one of the two independent Fe sites, Fe1, accompanied by a lowering of symmetry. Monoclinic jarosites consist of linear chains of Fe2-centered octahedra connected by corner-sharing SO_4 tetrahedra (Figure 1B; Grey et al., 2013; Scarlett et al., 2010) and they have been described as containing butlerite-like regions by Grey et al. (2011). The synthesis of monoclinic jarosites is favored at lower (80-120 °C) temperatures compared with rhombohedral jarosites, with the relative amount of the monoclinic phase increasing with increasing temperature. Both monoclinic jarosite and

natrojarosite can be synthesized in non-acidified solutions, although jarosite synthesis is easier in acidified (i.e., ≥ 1 M H_2SO_4) solutions (Grey et al., 2013; Scarlett et al., 2013; Scarlett et al., 2010). Monoclinic jarosite has been observed to transform to stoichiometric rhombohedral jarosite at ~250 °C, a significantly higher temperature than the non-stoichiometric to stoichiometric transition in rhombohedral jarosite (Grey et al., 2013). The volume thermal expansion of monoclinic natrojarosite during heating is of the same magnitude as that observed for rhombohedral jarosite but differs in value (Brand et al., 2017).

~Figure 1 here~

Here we present an analysis of the crystal structure and the thermal behaviour of seven samples of naturally occurring natrojarosite from Southside Beach in Victoria, Australia. Electron microscopy and electron backscatter diffraction were also done to investigate the spatial distribution of monoclinic versus rhombohedral natrojarosite in samples from Southside Beach.

EXPERIMENTAL METHODOLOGY

Field locality and sampling

Seven subsamples were collected from a natrojarosite-bearing cobble (64-256 mm) denoted Js-SB-35 located in the intertidal zone at Southside Beach in Victoria, Australia (E: 144.2732, N: 38.3740). Four of those subsamples, Js-SB-35A, -35B, -35E and -35F were part of the Whitworth et al. (2020) study. The other three subsamples denoted Js-SB-35G, -35H and -35I were obtained subsequently from the cobble as part of this investigation.

Room temperature PXRD

All subsamples were hand ground using an agate mortar and pestle, and jarosite was isolated from matrix materials (e.g., sediment, sand) using tweezers, picks and brushes while

viewing the samples under a hand specimen microscope. The seven subsamples were loaded into 0.3 mm diameter borosilicate glass capillaries and mounted onto the Powder Diffraction (PD) beamline (Wallwork et al., 2007) at the Australian Synchrotron. Capillaries were rotated at ~1 Hz during data collection to aid powder averaging. Diffraction patterns were collected over two beamtime allocations with the Mythen-II microstrip detector (Schmitt et al., 2003) at a wavelength of either 0.77448(1) Å or 0.590726(6) Å. The Mythen detector is a position sensitive detector with an inherent resolution of 0.004°. The instrument contribution to observed profiles and wavelength were determined using an XRD pattern collected from the NIST LaB_6 660b standard reference material using the fundamental parameters approach (Cheary and Coelho, 1992) within DIFFRAC.TOPAS 5 (Bruker). Two patterns, each of 300 s, were collected for each sample with the detector set 5° apart to cover the gaps between detector modules. The two patterns were then merged into a single dataset using the PDViPeR software available at the beamline. DIFFRAC.EVA (Bruker) was used to identify the minerals present in the samples using the Crystallography Open Database (Grazulis et al., 2009), and Rietveld refinement (Bish and Howard, 1988; Hill and Howard, 1987; Rietveld, 1969) as embodied in the TOPAS 5 software was used to model the structure of the minerals present.

Rietveld refinements of PXRD data collected at room temperature were performed starting from the structural model of the monoclinic natrojarosite from Scarlett et al. (2010). This structure was selected as peak shoulders and peak splitting suggestive of monoclinic symmetry were identified in the PXRD patterns (see the Room temperature PXRD results section for details). Natrojarosite peak shapes were modelled using a Thompson-Cox-Hasting pseudo-Voigt function (Thompson et al., 1987). Where elemental abundance data were known, the Na and K occupancy factors were fixed; otherwise, they were initially allowed to refine. Thermal

parameters were constrained for like atoms on similar/identical sites, i.e., Na and K, both Fe sites and O sites. Hydrogen positions and thermal parameters were set to values from Grey et al. (2011) and not refined due to the low X-ray scattering cross sections of light elements.

The peak shapes of accessory minerals were modelled with a Thompson-Cox-Hasting pseudo-Voigt function (Thompson et al., 1987) or a Pearson VII (PVII; Hall et al., 1977) function as appropriate. The unit-cell parameters of accessory phases were refined whereas their atomic positions, occupancies and thermal parameters were set to previously published values as they were not the focus of this study. Preferred orientation effects were identified for accessory minerals in several samples. These effects were modelled using spherical harmonics (Von Dreele, 1997).

In situ PXRD heating experiments

Grey et al. (2013) observed the transformation of synthetic monoclinic jarosite to stoichiometric rhombohedral jarosite during *in situ* PXRD heating experiments. As such, a separate set of heating experiments was undertaken at the Australian Synchrotron PD beamline to test whether this would occur with the natural monoclinic natrojarosite. Subsample Js-SB-35A was selected for the experiments because (1) monoclinic peak splitting of the natrojarosite was most evident in the PXRD patterns (see Figure 2), (2) refined Fe values reflected ordering of iron-site vacancies onto the Fe1 site at room temperature (see Supplemental Table S1 for the values), and (3) there was a sufficient amount of powder available to run multiple heating experiments. Subsamples were loaded in 0.7 mm silica glass capillaries, heated using a Cyberstar hot air blower and again rotated ~1 Hz during measurement. A temperature calibration curve for the instrument configuration used in these experiments was provided by the beamline team. The X-ray wavelength and instrument contributions were again determined using NIST LaB_6 660b.

The wavelength was 0.774800(3) Å. The sample was heated from 30-500 °C, at a rate of 5 °C/minute, and patterns were collected for 60 s in contiguous pairs to cover the gaps between detector modules.

The structure refined for monoclinic natrojarosite sample Js-SB-35A at room temperature was used as the starting point for Rietveld refinement of the heating datasets. As per the room temperature analyses, the natrojarosite peak shapes were modelled using a Thompson-Cox-Hasting pseudo-Voigt function (Thompson et al., 1987), the thermal parameters were constrained for like atoms on similar/identical sites, and the hydrogen positions and thermal parameters were set to values from Grey et al. (2011) and not refined.

The following procedure was used to ensure structure refinements were consistent at each heating time point: Firstly, the natrojarosite unit-cell parameters (i.e., *a*, *b*, *c* and β′) and Fe occupancy factors were refined. Next, the Beq values were allowed to refine. At this point, reflection-dependent peak broadening became apparent, and it was necessary to use the Stephens anisotropic line-shape broadening model, adapted for monoclinic symmetry (Stephens (1999)). Finally, the atomic coordinates for S and O were refined if any discrepancy still existed between the Rietveld refinement fit and PXRD pattern.

The structures of accessory mineral phases quartz and gypsum were refined for the initial room temperature dataset and then only their unit-cell parameters and preferred orientation parameters (where applicable) were refined at non-ambient temperatures. The phase composition of sample Js-SB-35A was determined using the quantitative phase analysis procedure in TOPAS 5 and the results are given in Table 1.

During Rietveld refinement, several small peaks were noted in a subset of the PXRD patterns. These peaks reflect sample impurities at or below the detection limit of the instrument

and could not be identified but they do not correspond to any of the potential phases expected to arise from decomposition of jarosite minerals.

Inductively coupled plasma-optical emission spectrometry.

The elemental composition of sample Js-SB-35A was determined using ICP-OES in order to constrain Na/K site occupancy during Rietveld refinements. An aliquot of powdered sample (20.0 ± 0.2 mg) was dissolved in 1 mL of 10 M HCl at 25 °C for 24 hours. The resulting solution was subsequently diluted to a concentration of 1 M HCl by adding 9 mL of ≥18.2 MΩ·cm MilliQ water. The solutions were then filtered (0.22 μm) to remove insoluble organic material. A small aliquot of the filtered solution was then further diluted to one tenth of the original concentration for ICP-OES analysis. Elemental concentrations for K, Na, Fe, Ca, and S were measured on a Thermo iCAP 7400 Duo ICP-OES in radial mode and were quantified by conversion of counts per second to ppm using calibration curves prepared using Fisher Chemical K, Na, Fe, Ca, and S standard solutions for ICP at known concentrations. The wt.% results for sample Js-SB-35A are given in Table 1.

Thermogravimetric analysis

Thermogravimetric analysis and differential thermal analysis (DTA) were performed using a Netzsch STA 449 F1 Jupiter Simultaneous TGA/DSC thermal analyzer. A powdered aliquot of Js-SB-35A (36 mg) was heated to 800 °C, at a heating rate of 10 °C/minute, under ultra-high purity argon that was purged at 40 mL/minute. A correction/blank was run prior to the sample to correct for the background. The results of the analysis are given in Table 1.

Electron backscatter diffraction and scanning electron microscopy

A portion of sample Js-SB-35 was mounted in epoxy resin and polished for electron backscatter diffraction (EBSD) and backscattered scanning electron (BSE) imaging using

facilities within Plymouth Electron Microscopy Centre, University of Plymouth, UK. EBSD analysis was conducted using a Zeiss Crossbeam 550 field-emission beam scanning electron microscope (FIB-SEM), using 15 kV accelerating voltage and 5 nA probe current. The EBSD detector was an Oxford Instruments Symmetry detector, using AZtec software v4.5 for data acquisition. The sample was mounted on a pre-titled sample holder held at 70°. Data acquisition utilised the sensitive mode and specified a Hough resolution of 60 and 11 bands, using 2x2 binning and an exposure time of 3.00 ms. A step size of 0.05 μm was used for mapping. The EBSD pattern was indexed using monoclinic natrojarosite unit-cell parameters from Scarlett et al. (2010) and rhombohedral natrojarosite unit-cell parameters from Basciano and Peterson (2008; sample P). Data were noise-reduced using Oxford Instruments AZtec Crystal software, using a 'wild-spike correction' to remove isolated data points between grains, followed by iterative eight- and seven-point nearest-neighbour zero solutions reduction so not to bias the dataset or introduce artefacts.

BSE images were collected using a JEOL 7001F field emission SEM at 15 kV accelerating voltage (probe current 10). Energy-dispersive spectroscopy (EDS) was used to determine elemental composition using an Oxford Instruments X-Max 50 mm^2 detector, and data were processed using Oxford Instruments AZtec software v4.3.

RESULTS

Room temperature PXRD

The room temperature PXRD patterns show that major natrojarosite and minor quartz (SiO_2) are present in all seven subsamples of Js-SB-35. Other crystalline accessory phases that were detected by PXRD include gypsum ($CaSO_4 \cdot 2H_2O$), halite (NaCl) and goethite (FeOOH). In

addition, a broad hump centred at d = 4.2 Å in some samples indicates the presence of an appreciable amorphous component. The absence of asymmetrical peak broadening and the sharpness of the 00l reflection of natrojarosite in these patterns suggests that there is only minor substitution of other elements (i.e., K) into the D site of natrojarosite (Figure 2A; Basciano and Peterson, 2007; Whitworth et al., 2020). This is consistent with the elemental chemistry of Js-SB-35A, -35B, -35E and -35F that was previously determined by Whitworth et al. (2020) using inductively coupled plasma-mass spectrometry (ICP-MS), and with the ICP-OES chemistry for Js-SB-35A reported in Table 1.

For all data collected at room temperature, the high-resolution nature of the synchrotron PXRD patterns enabled observation of peak shoulders and peak splitting suggestive of monoclinic symmetry. This is illustrated in Figures 2A and B, showing the splitting of the 012, 027 and 033 peaks of the rhombohedral structure into pairs of peaks or forming a clear peak shoulder. The magnitude of the splitting and the relative intensities of the pairs of peaks in Figure 2B are almost identical to those reported for synthetic monoclinic jarosite by Grey et al. 2013 (their Figure 2). Figures 2C and D show the same diffraction region for the rhombohedral natrojarosite Js-SB-38 from Whitworth et al. (2020), with no splitting of the 012, 027 and 033 peaks. It should be highlighted that asymmetrical peak broadening of the 003 peak due to substitution of K into the D-site of the natrojarosite (Whitworth et al., 2020) is visible in Figure 2C. Similar broadening is also apparent in the 027 peak in Figure 2D. Given the absence of observable splitting of the 012 and 033 peaks in Js-SB-38, and the measurement of multiple elements (e.g., Al, P) at minor to trace concentration (see Appendix A in Whitworth et al., 2020, for details) that are known to substitute into the jarosite structure, this broadening likely reflects the substitution of those elements into the crystal structure of the natrojarosite.

~Figure 2 here~

Mechanical mixing of synthetic monoclinic and rhombohedral jarosites has previously been observed by Scarlett et al. (2013). As such, the pattern of natrojarosite was first fitted with rhombohedral and monoclinic structures, separately and in the same refinement, as well as with multiple rhombohedral structures to determine which model gave the best fit to the observed data. Starting structures for monoclinic and rhombohedral jarosites were taken from Scarlett et al. (2010) and Basciano and Peterson (2008), respectively. The best fit to the data was observed using a monoclinic structure. For example, Js-SB-35A returned a residual weighted profile (R_{wp}) value of 4.44 % with an R_{Bragg} of 1.55 % using the monoclinic structure. This is compared with R_{wp} and R_{Bragg} values of 9.45 % and 6.08 %, respectively, using a single rhombohedral structure. Similarly, when two rhombohedral structures were employed in fitting, an R_{wp} value of 7.45 % was returned, with R_{Bragg} values of 7.34 % and 5.17 % being obtained using each of the two rhombohedral structures. Using a monoclinic and a rhombohedral structure in the same refinement resulted in semi-quantitative phase abundances of 20 wt.% rhombohedral and 80 wt.% monoclinic natrojarosites, with an R_{wp} of 4.75 %. Thus, the monoclinic structure provided the best fit to the observed data. In light of this result, and the observation of peak splitting indicative of monoclinic symmetry, detailed structural analysis proceeded with refinement of a single monoclinic structure.

The natrojarosite peaks were fitted with a C-centered monoclinic unit cell, space group *C*2/*m*, during Rietveld refinement and the results are reported in Table S1 (Supplemental Table). There are two independent iron atom sites in the *C*2/*m* model: Fe1 and Fe2 at 0, 0, ½ and ¾, ¼, ½, respectively. Rietveld refinement results show that iron vacancies occur preferentially in the Fe1 site for all seven samples which is characteristic of monoclinic jarosite (Grey et al., 2011;

Scarlett et al., 2010). The monoclinic unit cell was converted into a pseudohexagonal unit cell to further test the validity of the fit using the following transformations (Grey et al., 2013): $a_{ph} = \frac{1}{3}(2a/\sqrt{3} + b)$, $c_{ph} = (a^2 + 9c^2 + 6ac\cos\beta)^{1/2}$ and $\beta' = \cos^{-1}[(a^2 + c^2_{ph} - 9c^2)/2ac_{ph}]$. Table 2 reports the pseudohexagonal unit-cell parameters calculated for the seven natrojarosite samples at room temperature.

The amount of monoclinicity appears to vary between samples. For example, Js-SB-35A has clear peak splitting, iron site occupancies of 0.872(3) and 0.978(2) for Fe1 and Fe2, respectively, and a β′ value of 89.836(1)°. In comparison, sample Js-SB-35H does not have clear peak splitting or shoulders, and it has iron site occupancies of 0.854(8) and 0.970(4) for Fe1 and Fe2, respectively, and a β′ value of 89.904(2)°. These results suggest that a monoclinic model does not fit the data for Js-SB-35H as well as for Js-SB-35A. This suggests that structural heterogeneity exists within the natrojarosite subsampled from the larger cobble, Js-SB-35. The pseudohexagonal angle β′ ranges from 89.81 to 89.90° for the seven natural natrojarosite samples. For comparison, synthetic monoclinic jarosites have β′ in the range 89.65 to 89.76° when prepared from acidified solutions (1 M H_2SO_4), and in the range 89.83 to 89.96° when prepared from non-acidified solutions (Grey et al. 2013). The results for the natural monoclinic natrojarosites closely match the latter results for the synthetic jarosites, indicating close to neutral solutions during formation.

In Situ heating PXRD

Rietveld refinement with *in situ* PXRD data was used to monitor changes in the structure of natrojarosite from Southside Beach to see whether it undergoes thermal evolution similar to that described in earlier studies of synthetic monoclinic jarosites (Grey et al., 2013, Brand et al., 2017). In particular, we are interested in (1) whether the natrojarosite transitions from a

monoclinic structure to a stoichiometric rhombohedral structure; (2) the temperature at which that transition occurs, and (3) how the Fe sites behave.

Initially, the PXRD patterns were visually inspected for evidence of phase transitions using a version of Figure 3 that includes an extended 2θ range. Phases were identified using EVA and the Crystallography Open Database (COD).

~Figure 3 here~

Figure 3 shows a 2D overview of the diffraction data obtained during heating of Js-SB-35A from 30 to 500 °C. Major reflections assigned to each phase are labelled. A phase transition from gypsum to anhydrite ($CaSO_4$) can be observed between 130-140 °C, where gypsum peaks disappear as anhydrite peaks appear. Quartz is present throughout. Above 400 °C, the appearance of new peaks is observed in association with formation of natrojarosite decomposition products. Interestingly, there are no visible $FeOHSO_4$ peaks. During heating below ~200 °C, there is gradual movement of the natrojarosite reflections towards lower 2θ angles due to thermal expansion of the structure.

A change in the width and shape of the characteristic monoclinic, or "split", natrojarosite reflections occurs with temperature (Figure 4). There is a gradual loss of the 200_m peak shoulder until ~265-270 °C where there is an inflection point in the peak position that can be seen in Figure 5. This indicates that the β' angle of the natrojarosite has changed. Furthermore, it suggests that a symmetry change from monoclinic to rhombohedral has occurred as described by Grey et al. (2013). This is supported by a decrease in proportion of vacancies in the Fe1 site during heating (see below for details). However, this structural change seems to be a more gradual process in naturally occurring natrojarosite than the sharp change that has been observed in previous jarosite heating experiments that used synthetic minerals.

~Figure 4 here ~

~ Figure 5 here ~

Rietveld refinement results for heating experiments

Variation in the refined unit-cell volume with temperature is similar in magnitude to that observed for heating experiments using synthetic monoclinic natrojarosite done by Brand et al. (2017) but this sample expands at a slightly smaller rate. In general, there is a gradual change in the structure that is shown in Figure 6 where panel A shows the occupancy of the Fe sites and panel B the variation in the pseudo-hexagonal β' angle. The proportion of vacancies on the Fe1 site decreases towards the lower Fe2 value, which remains constant throughout heating. The pseudo-hexagonal β' value increases towards the rhombohedral value of 90° from about 130° C suggesting that iron is diffusing between the two Fe sites.

Datasets collected from 200-300 °C were also fitted with a rhombohedral structure to test the extent to which the ordering of iron-site vacancies was being lost. The profiles of natrojarosite in the dataset that correspond to the inflection in the peak profile, which was observed at 260 °C, are best fitted with a rhombohedral unit-cell of a = 7.3329(1) Å, c = 16.766(1) Å, which is consistent with values for the rhombohedral natrojarosite–hydronium jarosite solid solution described by (Basciano and Peterson, 2008). This temperature is also consistent with that previously observed by Grey et al. (2011) (220-270 °C) for the transition from non-stoichiometric monoclinic natrojarosite to stoichiometric rhombohedral natrojarosite.

~ Figure 6 here ~

Thermogravimetric analysis

Grey et al. (2011) showed that TGA can be used to elucidate the temperature of transformation of jarosites from monoclinic to rhombohedral symmetry. TGA and DTA data for

natrojarosite from Southside Beach show three main endotherms at 140, 390 and 668 °C (Figure 7). The first endotherm at 140 °C corresponds to loss of H_2O due to dehydration of gypsum, which was also seen in the PXRD data between 130 and 140 °C. The endotherm at 390 °C corresponds to H_2O loss due to dehydroxylation of iron-centered octahedra in natrojarosite, and this results in decomposition of the phase at ~400 °C, which is consistent with the absence of natrojarosite peaks in the PXRD pattern. The endotherm at 668 °C corresponds to SO_3 evolution during decomposition of sulfate associated with natrojarosite (Grey et al., 2013). Dehydroxylation of synthetic monoclinic jarosites together with loss of structural H_2O/H_3O^+ has been observed between 390 and 450 °C by several authors including Drouet and Navrotsky (2003), Grey et al. (2011, 2013) and Kubisz (1971); thus, the temperature of dehydroxylation here is comparable with the results of previous studies. The transition of the natrojarosite from monoclinic to rhombohedral symmetry, which was seen as an endotherm at ~280 °C by Grey et al. (2013) during the transformation of synthetic monoclinic jarosite to rhombohedral jarosite, was not observed in the TGA data. This may be due to the absence of butlerite-like regions in the natural natrojarosite samples, and this is discussed in more detail in the discussion section. Consistent with the results of Grey et al. (2011), dehydration and dehydroxylation mass losses were identified in the temperature ranges 30 to 280 and 280 to 550 °C, respectively, and are reported in Table 1.

~ Figure 7 here ~

Electron backscatter diffraction

Powder X-ray diffraction is a bulk technique; the structures obtained from refinements using PXRD data are an average for all crystallites of natrojarosite present in each subsample. We used room temperature PXRD to show that variations in the structure of natrojarosite exist

between subsamples collected from the cobble at Southside Beach. Structural heterogeneity of this type is common in naturally occurring mineral specimens. A thin section was prepared to investigate spatial variation in the structure of the natrojarosite within the cobble. Figure 8 shows a large field view of the thin section using BSE imaging. Regions with higher mean atomic number appear as very light grey areas and are mostly sediment (containing minerals including quartz, gypsum, ilmenite, and zircon) in a silica-rich cement, whereas the slightly darker grey areas contain natrojarosite or an admixture of natrojarosite and quartz. Figure 9 shows several regions of interest from across the thin section that were imaged at higher resolution than the whole thin-section image, including natrojarosite alongside gypsum, zircon, and REE-bearing phosphates. Figure 9A shows that the natrojarosite crystals present in the cobble are very small (<2 μm in the longest dimension) and have octahedral faces and a cubic habit. This morphology has been observed in low-temperature jarosites in acidic, sulfate-rich environments by several authors (e.g., Carson et al., 1982; Doner and Lynn, 1989; Wagner et al., 1982) and may suggest that the natrojarosite formed pseudomorphically after cubic pyrite. Figures 9B-D show accessory minerals that are present in Js-SB-35. In Figure 9B, tabular, striated gypsum crystals can be seen intermixed with the natrojarosite. Figures 9C and 9D show a zircon grain and a phosphate mineral, monazite, respectively, surrounded by jarosite crystals. These minerals were not observed in PXRD data because they occur in low abundance and because their distribution is heterogenous. As a result, they may not have been present in the subsamples collected from the cobble for PXRD analysis.

EBSD was conducted in the region enclosed by the white box in Figure 8, and Figure 10 shows one of the images collected within the region. Diffraction patterns obtained from grains in this region were indexed using both monoclinic and rhombohedral natrojarosite structures. The

grains that were not indexed are accessory minerals that can be identified as dark regions in Figure 10. Natrojarosite was indexed in one of three ways: (1) as monoclinic natrojarosite (predominantly purple), (2) as rhombohedral natrojarosite (predominantly blue), and (3) as either monoclinic or rhombohedral natrojarosite (mottled purple and blue). The natrojarosite grains exhibited a strong band contrast during EBSD analyses, indicating that they index very well against the respective natrojarosite structures. The mean angular deviation (MAD) values, which represent the level of misfit to the known pattern, for the rhombohedral and monoclinic jarosite phases in this region were low; 0.89 and 0.85 respectively. Thus, EBSD further demonstrates that monoclinic natrojarosite grains are dominant in Js-SB-35 and highlights that both monoclinic and rhombohedral natrojarosite occur in the cobble.

Quantitative analysis of the phases present in this region shows that 40.1% of the phases index as monoclinic natrojarosite, 16.3% index as rhombohedral jarosite; 43.6% do not index as monoclinic or rhombohedral natrojarosite, therefore representing other phases not of interest to this study such as the quartz, gypsum, and phosphates identified in Figure 9. EBSD analysis of this region therefore suggests the monoclinic natrojarosite is more prevalent than rhombohedral natrojarosite, similar to what was seen in the semi-quantitative phase analysis for Js-SB-35A using PXRD data. However, unlike the previous PXRD data, EBSD analysis can spatially resolve the proportion and location of monoclinic natrojarosite within Js-SB-35A.

~ Figure 8 here ~

~Figure 9 here~

~Figure 10 here~

DISCUSSION

Structural heterogeneity in Js-SB-35

In the room temperature PXRD data, variations in the amount of monoclinicity of the subsamples was detected. For example, Js-SB-35A has clear splitting of single peaks (e.g., 012, 027 and 033) of the rhombohedral structure into pairs of peaks in PXRD patterns, well-ordered iron-site vacancies and a pseudohexagonal β′ angle of 89.84°. In comparison, Js-SB-35H does not have clearly visible peak splitting or shoulders and has a pseudohexagonal β′ angle very close to 90° (89.9°). One explanation is that the amount of disordering of iron-site vacancies varies between subsamples, resulting in differences in the Fe1 and Fe2 occupancies, as well as the deviations away from a pseudo-hexagonal β' angle of 90°. A second explanation is that the differences in monoclinicity are a consequence of the subsamples being comprised of varying amounts of monoclinic and rhombohedral natrojarosite. As shown in the EBSD image (Figure 10), unambiguous regions of monoclinic and rhombohedral natrojarosite are present in the cobble, as well as regions that can be described using either model. This suggests that these regions are intermixed monoclinic and rhombohedral natrojarosite. Subsamples such as Js-SB-35A likely represent regions in the EBSD image describable only by a monoclinic model. Conversely, subsamples such as Js-SB-35H most likely represent regions in the EBSD image that can be described using both a monoclinic and rhombohedral model reflecting the presence of both monoclinic and rhombohedral natrojarosite in this subsample. The PXRD data for all subsamples are still most consistent with a monoclinic model, suggesting that there is more monoclinic natrojarosite in the samples than rhombohedral natrojarosite. This is supported by quantitative phase analysis of the region analysed using EBSD, giving a mean ratio of 2:1 across the thin section. Structural and chemical heterogeneity clearly exist within natrojarosite in Js-SB-

35. This highlights the importance of collecting and analysing multiple samples when investigating natural jarosites.

Structural formula of natural monoclinic natrojarosite

The Rietveld refinements using synchrotron PXRD data for seven monoclinic natrojarosite samples (supplemental table S1) give remarkably small variations in the structural formulae. The Na/K distribution in the D site varies in the range of $Na_{0.88}K_{0.12}$ to $Na_{0.98}K_{0.02}$, and the total Fe site vacancy varies from 0.13 to 0.21 per formula unit. The mean structural formula is: $Na_{0.92}K_{0.08}Fe_{2.83}(SO_4)_2(OH)_{5.49}(H_2O)_{0.51}$. The formula for sample Js-SB-35A, for which TGA and ICP-OES data are available (Table 1) is $Na_{0.95}K_{0.05}Fe_{2.83}(SO_4)_2(OH)_{5.49}(H_2O)_{0.51}$. Based on this formula the excess H_2O content (associated with Fe vacancies) is 1.9 wt.% and hydroxyl ions comprise 10.4 wt.%. For comparison, the amount of H_2O lost via dehydration and dehydroxylation during TGA are 1.6 and 12.1 wt.%, respectively. The amount of excess H_2O detected using TGA is much closer to the Kubitz (1970,1971) model for non-stoichiometric jarosites (1.9 wt.%), which has each Fe(III)-site vacancy charge compensated by protonation of $3OH^-$ to $3H_2O$, than to the alternative Nielson et al. (2008) model [each Fe(III)-site vacancy charge compensated by protonation of $4OH^-$ to $4H_2O$, with one proton coming from coupled deprotonation of a D-site H_3O^+ molecule] which would require 2.5 wt.% H_2O. This result is consistent with the ICP-OES results, which suggest that the natural natrojarosite samples do not have substitution of hydronium ion at the D site. In contrast, synthetic natrojarosites all have substantial (~30%) replacement of Na^+ by H_3O^+, and the excess H_2O contents of the synthetic samples are more consistent with the Nielsen model (Nielson et al., 2008).

The measured hydroxyl content, 12.1 wt.%, is greater than the value of 10.4 wt.% indicated by the structural formula determined as part of this study. A possible explanation for

this discrepancy is that the sample contains amorphous iron oxyhydroxide. The PXRD data for sample Js-SB-35A show a broad hump centred at d ~ 4.2 Å which is where the most intense goethite peak occurs. The ICP-OES analyses for Js-SB-35A (Table 1), normalised to 2 SO_4 per formula unit, give a formula $Na_{0.95}K_{0.05}Fe_{3.46}(SO_4)_2(OH)_{7.38}$, with excess Fe and OH compared with the structural formula. These observations are consistent with the natural natrojarosite containing about 10 wt.% of amorphous iron oxyhydroxide.

Thermal behaviour and properties of natural natrojarosite

Structural modelling of hydrothermally synthesised natrojarosite and hydronium jarosites by Grey et al. (2011) showed that these samples were comprised of domains of butlerite-like $[Fe_2(SO_4)_2(OH)_2(H_2O)_4]$ chains within the stoichiometric jarosite. Thermal analysis of these jarosites detected an endotherm below 280 °C that was attributed to the formation of $FeOHSO_4$ due to the dehydration of domains with butlerite-like chains. Similar endotherms have also been detected during thermal analysis of synthetic jarosites by Drouet and Navrotsky (2003), Grey et al. (2013) and Kubisz (1971). We did not observe this endotherm, nor was $FeOHSO_4$ seen in the PXRD data, suggesting that the domains of butlerite-like chains are very small and disconnected or do not exist in the natural samples. Thus, the Fe-site vacancies may be more randomly distributed in the natural monoclinic sample.

Structural transformation of natural monoclinic natrojarosite with increasing temperature appears to be more gradual than synthetic jarosite minerals. There are several possible explanations for this. Firstly, the more random distribution of Fe-site vacancies in the natural sample compared to synthetic samples with butlerite-like domain may slow the rate of Fe diffusion during heating, making the transformation more gradual. A second possible explanation is that differences in hydrogen bonding may be causing the more gradual

transformation. The thermal behaviour of monoclinic natrojarosite is closely related to hydrogen bonding within the structure (Brand et al., 2017). Hydrogen bonding is expected to vary between monoclinic and rhombohedral jarosites. Therefore, it can be expected that the thermal behaviours of monoclinic and rhombohedral jarosites will vary. This was seen by Brand et al. (2017) where the volume thermal expansion of monoclinic natrojarosite during heating is of the same order of magnitude (i.e., 10^{-5} K^{-1}) but larger in value compared with rhombohedral jarosite. A third possible explanation is that the structural heterogeneity present in the natural sample resulted in the transformation being more gradual.

Formation of natural monoclinic natrojarosite

Numerous studies (e.g., Alpers et al., 1992; Chen et al., 2013; Desborough et al., 2010; Mills et al., 2013; Whitworth et al., 2020) have examined the crystallography of natural jarosites, reporting only rhombohedral symmetry. In contrast, the results of this study demonstrate that monoclinic natrojarosite can form in a natural environment, which raises questions as to why monoclinic symmetry has not been observed in other natural jarosite samples before.

One explanation for the lack of reported monoclinic symmetry could be that the resolutions of the diffraction instruments used in many of the earlier studies were not sufficient to resolve the subtle peak splitting associated with monoclinic symmetry. Peak splitting was almost undetectable in several of the room temperature PXRD patterns described here. This is not the first time that the resolution of X-ray diffractometers used in crystal structure analysis has been suggested as a reason for the apparent absence of natural monoclinic jarosites (see Grey et al., 2011), and further highlights the need for suitable data collection strategies when examining the crystal structures of jarosites.

529 A second possibility is that the formation conditions required to produce monoclinic
530 jarosite rarely occur in nature. Hydrothermal syntheses of monoclinic jarosites require low
531 temperatures (80 °C to 120 °C), solutions with [Fe]/[D site] atomic ratios ≥ 1, and relatively slow
532 growth conditions to stabilize the monoclinic phase (Grey et al., 2011, 2013; Scarlett et al.,
533 2010). Natural hydrothermal jarosites typically form at temperatures ranging from 100-300 °C
534 (Desborough et al., 2010). Thus, hydrothermal jarosites may form at temperatures too high for
535 monoclinic symmetry. Supergene jarosites, on the other hand, form in cooler conditions that may
536 be more suitable for development of monoclinic symmetry, and the presence of monoclinic
537 jarosite in the low-temperature cobble studied here supports this. Natural jarosites also
538 commonly form at redox boundaries in physically dynamic environments such intertidal zones,
539 weathering horizons and geothermal systems (Desborough et al., 2010; Lueth et al., 2005;
540 Whitworth et al., 2020). These environments are likely not conducive to slow jarosite growth,
541 favoring rhombohedral symmetry, as suggested by Grey et al., 2011. However, the jarosite
542 analyzed in this study was sampled from a cobble collected from an environment (i.e., intertidal
543 zone) where rapid formation would be favored. This may suggest that growth rate is not as
544 strong a factor in formation of monoclinic symmetry in jarosites as previously suggested.
545 A third possible explanation for the scarcity of monoclinic jarosites in natural settings is
546 that when monoclinic jarosite forms in a natural setting it transforms to rhombohedral jarosite
547 through the diffusion of iron between the two iron sites. Grey et al. (2013) found in their
548 experiments that when monoclinic jarosites were exposed to temperatures ≥100 °C for prolonged
549 periods they progressively converted to rhombohedral symmetry. Our experiments also show
550 that heating monoclinic natrojarosite over short (i.e., few hours) timeframes causes gradual
551 transformation from monoclinic to rhombohedral symmetry above 150 °C. Thus, monoclinic

552 natural jarosites exposed to temperatures of 100 °C or greater for prolonged periods of time, or
553 monoclinic jarosites that experience even short periods of heating above 150 °C, are likely to
554 transform to rhombohedral symmetry through iron diffusion. Iron diffusion may be occurring
555 through a vacancy-filling mechanism. Energy is required for an atom to move to a vacant site in
556 a structure. Heating of the jarosite results in more energy becoming available for the iron to
557 move into one of the Fe1 site vacancies. Thus, heating of the jarosite provides the iron atoms
558 with enough energy to diffuse into vacant sites. It is therefore not surprising that monoclinic
559 symmetry has not be observed in natural hydrothermal jarosites. Transformation of monoclinic
560 to rhombohedral symmetry in jarosites has not been examined at low temperature. However, the
561 presence of monoclinic symmetry in cobble studied here would suggest that monoclinic
562 symmetry can persist in low temperature jarosites. One possible explanation for this is that the
563 lower temperature of the natural environment is resulting in less energy being available for Fe
564 diffusion into vacant sites, slowing the rate of Fe diffusion. Thus, the presence of monoclinic
565 natrojarosite documented here may be the result of a combination of specific conditions (i.e., a
566 solution with an [Fe]/[Na] atomic ratios ≥ 1 favoring monoclinic formation and low temperatures
567 inhibiting Fe diffusion), although it seems more likely that natural monoclinic jarosites have not
568 been detected in earlier studies due to insufficient X-ray diffraction resolution.
569

570 **IMPLICATIONS**

571 This study has described the first observation monoclinic symmetry in naturally-
572 occurring jarosite and suggests that natural monoclinic jarosites may be more common than
573 previously thought. It is also likely that the presence of monoclinic symmetry will result in
574 natural monoclinic jarosites having somewhat different chemical compositions and physical

properties compared with natural rhombohedral jarosites. Further research on the formation conditions and physical (e.g., thermal, magnetic) differences between natural monoclinic and rhombohedral jarosites is therefore recommended. Understanding the complexities of natural jarosites could not only shed light on the formation conditions and environmental histories of jarosite outcrops on Earth and Mars but would be valuable knowledge for the management and utilization of jarosites in the environment and mineral processing.

A caveat to this is that it is currently unclear how common monoclinic jarosites are in nature. High-resolution synchrotron PXRD data are required to resolve the subtle peak splitting associated with monoclinic symmetry, which are not always available. This may make resolving this question using laboratory-based PXRD data alone challenging. However, this study has also demonstrated that EBSD, which is commonly available in university laboratories, is an effective technique for distinguishing between monoclinic and rhombohedral jarosite grains when they co-occur as admixtures in natural samples. This may occur frequently in natural jarosites, making EBSD a good tool for investigating the prevalence of monoclinic jarosites in nature. The data set provided here will be a valuable tool in the interpretation of future studies on the crystal structure of natural jarosites.

ACKNOWLEDGEMENTS

The authors would like to thank AINSE Limited for providing financial assistance (Award-PGRA) to AJW to enable work on this research. This work was also supported by a Faculty of Science Dean's Postgraduate Research Scholarship to AJW. Massimo Raveggi is thanked for ICP-OES measurements. Part of this work was carried out on the Powder Diffraction beamline at the Australian synchrotron.

598

599 **REFERENCES CITED**

600 Alpers, C.N., Rye, R.O., Nordstrom, D.K., White, L.D., and King, B.S. (1992) Chemical,
601 crystallographic and stable isotopic properties of alunite and jarosite from acid-
602 hypersaline Australian lakes. Chemical Geology, 96, 203-226.
603 Arregui, V., Gordon, A., and Steintveit, G. (1980) The jarosite process-past, present and future.
604 In J.M. Cigan, T.S. Mackey, and T.J. O'Keefe, Eds. Lead-Zinc-Tin'80, p. 97-123. TMS-
605 AIME, Warrendale, PA.
606 Asta, M.P., Cama, J., Martínez, M., and Giménez, J. (2009) Arsenic removal by goethite and
607 jarosite in acidic conditions and its environmental implications. Journal of Hazardous
608 Materials, 171(1-3), 965-72.
609 Basciano, L.C., and Peterson, R.C. (2007) Jarosite hydronium jarosite solid-solution series with
610 full iron site occupancy: Mineralogy and crystal chemistry. American Mineralogist, 92(8-
611 9), 1464-1473.
612 -. (2008) Crystal chemistry of the natrojarosite-jarosite and natrojarosite-hydronium jarosite
613 solid-solution series: A synthetic study with full Fe site occupancy. American
614 Mineralogist, 93(5-6), 853-862.
615 Bayliss, P., Kolitsch, U., Nickel, E.H., and Pring, A. (2010) Alunite supergroup: recommended
616 nomenclature. Mineralogical Magazine, 74(05), 919-927.
617 Bish, D.L., and Howard, S.A. (1988) Quantitative phase analysis using the Rietveld method.
618 Journal of Applied Crystallography, 21(2), 86-91.
619 Brand, H.E.A., Scarlett, N.V.Y., and Grey, I.E. (2012) In situ studies into the formation kinetics
620 of potassium jarosite. Journal of Applied Crystallography, 45(3), 535-545.

621 Brand, H.E.A., Scarlett, N.V.Y., and Knight, K.S. (2017) Thermal expansion of deuterated
622 monoclinic natrojarosite; a combined neutron–synchrotron powder diffraction study.
623 Journal of Applied Crystallography, 50(2), 340-348.
624 Carson, C.D., Fanning, D.S., and Dixon, J.B. (1982) Alfisols and Ultisols with Acid Sulfate
625 Weathering Features in Texas. Acid Sulfate Weathering, 127-146.
626 Cheary, R.W., and Coelho, A. (1992) A fundamental parameters approach to X-ray line-profile
627 fitting. Journal of Applied Crystallography, 25(2), 109-121.
628 Chen, L., Li, J.-W., Rye, R.O., Benzel, W.M., Lowers, H.A., and He, M.-Z. (2013)
629 Mineralogical, chemical, and crystallographic properties of supergene jarosite-group
630 minerals from the Xitieshan Pb-Zn sulfide deposit, northern Tibetan Plateau, China.
631 Mineralogy and Petrology, 107(4), 487-499.
632 Desborough, G.A., Smith, K.S., Lowers, H.A., Swayze, G.A., Hammarstrom, J.M., Diehl, S.F.,
633 Leinz, R.W., and Driscoll, R.L. (2010) Mineralogical and Chemical Characteristics of
634 Some Natural Jarosites. Geochimica et Cosmochimica Acta, 74, 1041-1056.
635 Doner, H.E., and Lynn, W.C. (1989) Carbonate, Halide, Sulfate, and Sulfide Minerals. Minerals
636 in Soil Environments, 279-330.
637 Drouet, C., and Navrotsky, A. (2003) Synthesis, characterization, and thermochemistry of K-Na-
638 H_3O jarosites. Geochimica et Cosmochimica Acta, 67(11), 2063-2076.
639 Dutrizac, J.E. (1983) Factors affecting alkali jarosite precipitation. Metallurgical Transactions B,
640 14B, 531-539.
641 Egal, M., Elbaz-Poulichet, F., Casiot, C., Motelica-Heino, M., Négrel, P., Bruneel, O.,
642 Sarmiento, A.M., and Nieto, J.M. (2008) Iron isotopes in acid mine waters and iron-rich

643 solids from the Tinto–Odiel Basin (Iberian Pyrite Belt, Southwest Spain). Chemical
644 Geology, 253(3-4), 162-171.
645 Frunzke, J., Hansen, T., Harrison, A., Lord, J.S., Oakley, G.S., Visser, D., and Wills, A.S. (2001)
646 Magnetic ordering in diluted kagome antiferromagnets. Journal of Materials Chemistry,
647 11(1), 179-185.
648 Gottlicher, J., Gasharova, B., and Bernotat-Wulf, H. (2000) Pseudotrigonal jarosites
649 $(K,H_2O)Fe_3(SO_4)_2(OH)_6$. Geological Society of America, Abstracts with programs, 32, p.
650 A180.
651 Grazulis, S., Chateigner, D., Downs, R.T., Yokochi, A.T., Quiros, M., Lutterotti, L., Manakova,
652 E., Butkus, J., Moeck, P., and Le Bail, A. (2009) Crystallography Open Database- an
653 open-access collection of crystal structure. Journal of Applied Crystallography, 42, 726-
654 729.
655 Grey, I.E., Scarlett, N.V.Y., Bordet, P., and Brand, H.E.A. (2011) Jarosite–butlerite intergrowths
656 in non-stoichiometric jarosites: crystal chemistry of monoclinic natrojarosite–
657 hydroniumjarosite phases. Mineralogical Magazine, 75(6), 2775-2791.
658 Grey, I.E., Scarlett, N.V.Y., and Brand, H.E.A. (2013) Crystal chemistry and formation
659 mechanism of non-stoichiometric monoclinic K-jarosites. Mineralogical Magazine,
660 77(3), 249-268.
661 Grohol, D., Nocera, D.G., and Papoutsakis, D. (2003) Magnetism of pure iron jarosites. Physical
662 Review B, 67(6), 064401.
663 Hall, M.M., Jnr, Veeraraghavan, V.G., Rubin, H., and Winchell, P.G. (1977) The approximation
664 of symmetric X-ray peaks by Pearson type VII distributions. Journal of Applied
665 Crystallography, 10(1), 66-68.

666 Hill, R.J., and Howard, C.J. (1987) Quantitative phase analysis from neutron powder diffraction
667 data using the Rietveld method. Journal of Applied Crystallography, 20(6), 467-474.
668 Jamieson, H.E., Robinson, C., Alpers, C.N., Nordstrom, D.K., Poustovetov, A., and Lowers,
669 H.A. (2005) The composition of coexisting jarosite-group minerals and water from the
670 Richmond mine, Iron Mountain, California. Canadian Mineralogist, 43, 1225-1242.
671 Johnston, S.G., Keene, A.F., Burton, E.D., Bush, R.T., Sullivan, L.A., McElnea, A.E., Ahern,
672 C.R., Smith, C.D., Powell, B., and Hocking, R.K. (2010) Arsenic Mobilization in a
673 Seawater Inundated Acid Sulfate Soil. Environmental Science & Technology, 44(6),
674 1968-1973.
675 Jones, A.M., Collins, R.N., Rose, J., and Waite, T.D. (2009) The effect of silica and natural
676 organic matter on the Fe(II)-catalysed transformation and reactivity of Fe(III) minerals.
677 Geochimica et Cosmochimica Acta, 73(15), 4409-4422.
678 Karimian, N., Johnston, S.G., and Burton, E.D. (2017) Antimony and Arsenic Behavior during
679 Fe(II)-Induced Transformation of Jarosite. Environmental Science & Technology, 51(8),
680 4259-4268.
681 Klingelhöfer, G., Morris, R.V., Bernhardt, B., Schröder, C., Rodionov, D.S., de Souza, P.A., Jr.,
682 Yen, A., Gellert, R., Evlanov, E.N., Zubkov, B., Foh, J., Bonnes, U., Kankeleit, E.,
683 Gütlich, P., Ming, D.W., Renz, F., Wdowiak, T., Squyres, S.W., and Arvidson, R.E.
684 (2004) Jarosite and Hematite at Meridiani Planum from Opportunity's Mössbauer
685 Spectrometer. Science, 306(5702), 1740-5.
686 Kubisz, J. (1970) Studies on synthetic alkali-hydronium jarosite. I. Synthesis of jarosite and
687 natrojarosite. Mineralogia Polonica, 1, 47-57.

-. (1971) Studies of synthetic alkali-hydronium jarosites. II. Thermal investigations. Mineralogia Polonica, 2, 51-59.

Langmuir, D. (1997) Aqueous Environmental Geochemistry. Prentice Hall, Upper Saddle River, New Jersey.

Liu, Y., Goudge, T.A., Catalano, J.G., Wang, A. (2018) Spectral and stratigraphic mapping of hydrated minerals associated with interior layered deposits near the southern wall of Melas Chasma, Mars. Icarus, 302, 62-79.

Lueth, V.W., Rye, R.O., and Peters, L. (2005) "Sour gas" hydrothermal jarosite: ancient to modern acid-sulfate mineralization in the southern Rio Grande Rift. Chemical Geology, 215(1-4), 339-360.

Majzlan, J., Glasnák, P., Fisher, R.A., White, M.A., Johnson, M.B., Woodfield, B., and Boerio-Goates, J. (2010) Heat capacity, entropy, and magnetic properties of jarosite-group compounds. Physics and Chemistry of Minerals, 37(9), 635-651.

Mills, S.J., Nestola, F., Kahlenberg, V., Christy, A.G., Hejny, C., and Redhammer, G.J. (2013) Looking for jarosite on Mars: The low-temperature crystal structure of jarosite. American Mineralogist, 98(11-12), 1966-1971.

Nishiyama, M., Maegawa, S., Inami, T., and Oka, Y. (2003) Magnetic ordering and spin dynamics in potassium jarosite: A Heisenberg kagomé lattice antiferromagnet. Physical Review B, 67.

Öborn, I., and Berggren, D. (1995) Characterization of jarosite-natrojarosite in two northern Scandinavian soils. Geoderma, 66, 213-225.

Rampe, E.B., Ming, D.W., Blake, D.F., Bristow, T.F., Chipera, S.J., Grotzinger, J.P., Morris, R.V., Morrison, S.M., Vaniman, D.T., Yen, A.S., Archilles, C.N., Craig, P.I., Des Marais,

711 D.J. (2017) Mineralogy of an ancient lacustrine mudstone succession from the Murray
712 formation, Gale crater, Mars. Earth and Planetary Science Letters, 471, 172-185.
713 Rampe, E. B., Bristow, T. F., Morris, R. V., Morrison, S. M., Achilles, C. N., Ming, D. W.,
714 Vaniman, D. T., Blake, D. F., Tu, V. M., Chipera, S. J., Yen, A. S., Peretyazhko, T. S.,
715 Downs, R. T., Hazen, R. M., Treiman, A. H., Grotzinger, J. P., Castle, N., Craig, P. I.,
716 Des Marais, D. J., Thorpe, M. T., Walroth, R. C., Downs, G. W., Fraeman, A. A.,
717 Siebach, K. L., Gellert, R., Lafuente, B., McAdam, A. C., Meslin, P.-Y., Sutter, B.,
718 Salvatore, M. R. (2020) Mineralogy of Vera Rubin Ridge From the Mars Science
719 Laboratory CheMin Instrument. Journal of Geophysical Research: Planets, 125(9).
720 Rietveld, H.M. (1969) A Profile Refinement Method for Nuclear and Magnetic Structures.
721 Journal of Applied Crystallography, 2, 65-71.
722 Sandström, Å., Shchukarev, A., and Paul, J. (2005) XPS characterisation of chalcopyrite
723 chemically and bio-leached at high and low redox potential. Minerals Engineering, 18(5),
724 505-515.
725 Savage, K.S., Bird, D.K., and O'Day, P.A. (2005) Arsenic speciation in synthetic jarosite.
726 Chemical Geology, 215(1-4), 473-498.
727 Scarlett, N.V., Grey, I.E., and Brand, H.E. (2013) In situ synchrotron diffraction studies on the
728 formation kinetics of jarosites. Journal of Synchrotron Radiation, 20, 366-75.
729 Scarlett, N.V.Y., Grey, I.E., and Brand, H.E.A. (2010) Ordering of iron vacancies in monoclinic
730 jarosites. American Mineralogist, 95(10), 1590-1593.
731 Schmitt, B., Bronnimann, C., Eikenberry, E.F., Gozzo, F., Hoermann, C., Horisberger, R.P., and
732 Patterson, B. (2003) Mythen detector system. Nuclear Instruments and Methods in

733 Physics Research Section A: Accelerators, Spectrometers, Detectors and Associated
734 Equipment, 501(1), 267-272.
735 Smith, A.M.L., Dubbin, W.E., Wright, K., and Hudson-Edwards, K.A. (2006a) Dissolution of
736 lead- and lead–arsenic-jarosites at pH 2 and 8 and 20 °C: Insights from batch
737 experiments. Chemical Geology, 229(4), 344-361.
738 Smith, A.M.L., Hudson-Edwards, K.A., Dubbin, W.E., and Wright, K. (2006b) Dissolution of
739 jarosite [$KFe_3(SO_4)_2(OH)_6$] at pH 2 and 8: Insights from batch experiments and
740 computational modelling. Geochimica et Cosmochimica Acta, 70(3), 608-621.
741 Stephens, P.W. (1999) Phenomenological model of anisotropic peak broadening in powder
742 diffraction. Journal of Applied Crystallography, 32, 281-289.
743 Stoffregen, R.E., Alpers, C.N., and Jambor, J.L. (2000) Alunite-Jarosite Crystallography,
744 Thermodynamics, and Geochronology. Reviews in Mineralogy and Geochemistry, 40(1),
745 453-479.
746 Stott, M.B., Watling, H.R., Franzmann, P.D., and Sutton, D. (2000) The role of iron-hydroxy
747 precipitates in the passivation of chalcopyrite during bioleaching. Minerals Engineering,
748 13(10-1), 1117-1127.
749 Thompson, P., Cox, D.E., and Hastings, J.B. (1987) Rietveld refinement of Debye-Scherrer
750 synchrotron X-ray data from Al_2O_3. Journal of Applied Crystallography, 20, 79-83.
751 Von Dreele, R.B. (1997) Quantitative texture analysis by Rietveld refinement. Journal of
752 Applied Crystallography, 30(4), 517-525.
753 Wagner, D.P., Fanning, D.S., Foss, J.E., Patterson, M.S., and Snow, P.A. (1982) Morphological
754 and Mineralogical Features Related to Sulfide Oxidation under Natural and Disturbed
755 Land Surfaces in Maryland. Acid Sulfate Weathering, 109-125.

Wallwork, K.S., Kennedy, B.J., and Wang, D. (2007) The High Resolution Powder Diffraction Beamline for the Australian Synchrotron. AIP Conference Proceedings, 879(1), 879-882.

Welch, S.A., Christy, A.G., Kirste, D., Beavis, S.G., and Beavis, F. (2007) Jarosite dissolution I — Trace cation flux in acid sulfate soils. Chemical Geology, 245(3-4), 183-197.

Whitworth, A.J., Brand, H.E.A., Wilson, S.A., and Frierdich, A.J. (2020) Iron isotope geochemistry and mineralogy of jarosite in sulfur-rich sediments. Geochimica et Cosmochimica Acta, 270, 282-295.

Wills, A.S., Harrison, A., Ritter, C., and Smith, R.I. (2000) Magnetic properties of pure and diamagnetically doped jarosites: Model kagomé antiferromagnets with variable coverage of the magnetic lattice. Physical Review B, 61(9), 6156-6169.

766 **LIST OF FIGURE CAPTIONS**

767 Figure 1. Illustration of the crystal structure of jarosite viewed along the c-axis, [001]. (A)
768 Rhombohedral jarosite with iron octahedra (green) and sulfate tetrahedra (yellow) shown. (B)
769 Monoclinic jarosite symmetry with the two iron octahedra sites (site one = blue, site two =
770 green) and sulfate tetrahedra (yellow) shown.

771

772 Figure 2. Representative PXRD patterns with only selected peaks shown. (A,B) Js-SB-35A, a
773 monoclinic natrojarosite sample. (C,D) Js-SB-38, a rhombohedral jarosite sample previously
774 described by Whitworth et al. (2020). The solid black arrows in Figures 2A and B indicate the
775 location of pairs of peaks resulting from splitting of the 012, 027 and 033 peaks of the
776 rhombohedral structure. The un-split 012 is shown in Figure 2C, and the un-split 027 and 033
777 peaks are shown in Figure 2D. The dotted arrow highlights asymmetrical peak broadening due to
778 minor K substitution in Js-SB-38. Subscript m and h indicate that the indices are monoclinic and
779 hexagonal, respectively

780

781 Figure 3. Partial PXRD pattern as a function of temperature for *in situ* decomposition of Js-SB-
782 35A natrojarosite (J). Accessory phases present include quartz (Q), gypsum (G), and anhydrite
783 (An).

784

785 Figure 4. Partial XRD pattern of Js-SB-35A showing gradual loss of peak shoulders with
786 increasing temperature. Patterns are at room temperature, 150, 175, 200 and 300°C. Peak
787 associated with anhydrite (An) noted.

788

Figure 5. Partial PXRD pattern as a function of temperature for in situ decomposition of Js-SB-35A natrojarosite. The transformation from monoclinic (M) to rhombohedral (R) natrojarosite is indicated. A peak associated with quartz is noted.

Figure 6. Panel A, Plot of Fe site occupancy against temperature. Fe1 site is shown with filled circles, Fe2 site is shown with crosses. Panel B, variation of the pseudo-hexagonal β′ angle with temperature. Error bars are approximately the size of the symbols.

Figure 7. Thermogravimetric analysis (red) and differential thermal analysis (blue) curves for Js-SC-35A. The temperatures of the endothermic peak maxima are given.

Figure 8. Large field of view of the thin section from Js-SB-35 using BSE imaging. The white box encloses the area that EBSD was conducted.

Figure 9. BSE images of Js-SB-35. (A) Pseudocubic natrojarosite crystals. (B) Tabular, striated gypsum intermixed with pseudocubic natrojarosite. (C) A rounded, zircon crystal surrounded by natrojarosite (light grey) and quartz (darker grey and rounded) crystals (D) A phosphate mineral surrounded by finer-grained natrojarosite and quartz crystals.

Figure 10. EBSD image of the thin section of Js-SB-35A highlighting regions that index as monoclinic natrojarosite (M; purple), rhombohedral natrojarosite (R; blue), or can be indexed using either a monoclinic or rhombohedral model (I; mottled blue and purple). Black regions correspond to accessory phases.

812 **TABLES**

813 Table 1. Characterisation of sample Js-SB-35A

ICP-OES results (wt.%)	Na	K	Ca	Fe	S	
	3.78	0.30	2.07	30.2	11.7	
Quantitative phase analysis (wt.%)	84.0 (±1)% natrojarosite		8.0 (±1) % gypsum		8.0 (±1) % quartz	
TGA endotherm peaks (°C)	140		390		668	
	30-280 °C, dehydration		280-550 °C, dehydroxylation		550-800 °C SO_3 loss	
Mass losses (wt.%) total	2.7		10.2		17.2	
For natrojarosite*	1.6		12.1		20.4	

814 *Corrected for dehydration of gypsum and percentage of natrojarosite in sample.

815

816
817
818 Table 2. Pseudohexagonal unit-cell parameters for natrojarosite at room temperature.

Sample	Js-SB-35A	Js-SB-35B	Js-SB-35E	Js-SB-35F	Js-SB-35G	Js-SB-35H	Js-SB-35I
a_{ph} (Å)	7.3256(1)	7.3247(1)	7.3264(1)	7.3261(1)	7.3253(1)	7.3204(1)	7.3237(1)
c_{ph} (Å)	16.6393(1)	16.6386(1)	16.6557(1)	16.6551(1)	16.6514(2)	16.6743(2)	16.6329(1)
β′ (°)	89.836(1)	89.847(1)	89.810(1)	89.846(1)	89.853(2)	89.904(2)	89.872(1)

819

820

This is the peer-reviewed, final accepted version for American Mineralogist, published by the Mineralogical Society of America.
The published version is subject to change. Cite as Authors (Year) Title. American Mineralogist, in press.
DOI: https://doi.org/10.2138/am-2022-8276. http://www.minsocam.org/

Figure 1

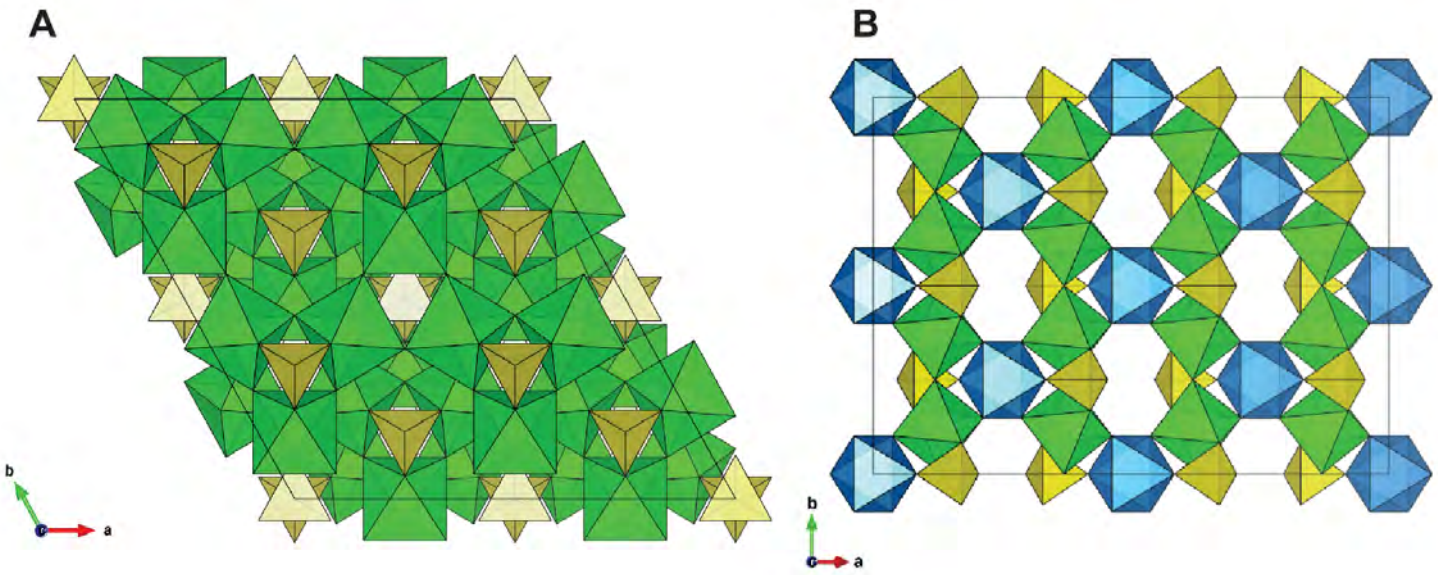

Figure 2

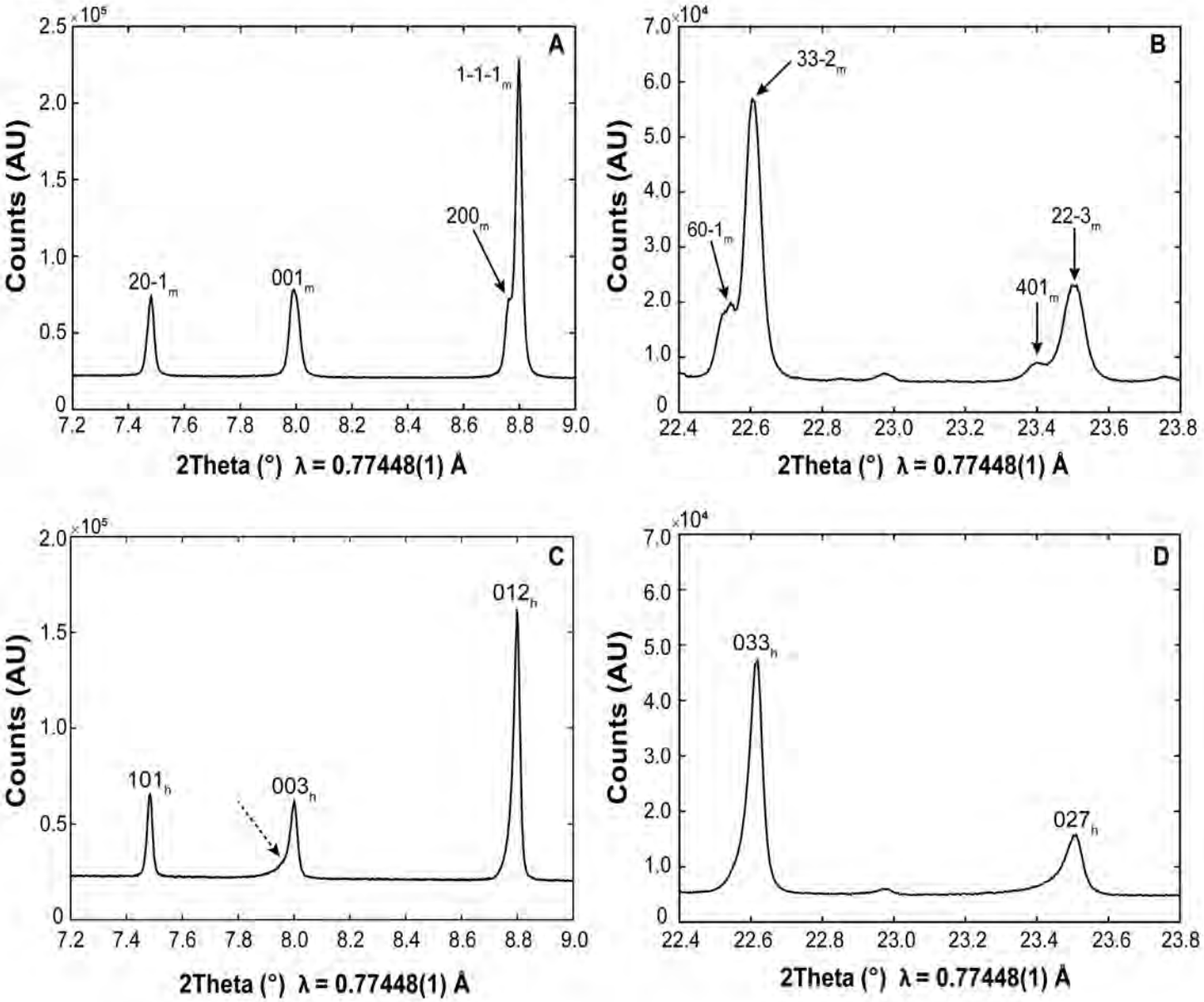

This is the peer-reviewed, final accepted version for American Mineralogist, published by the Mineralogical Society of America.
The published version is subject to change. Cite as Authors (Year) Title. American Mineralogist, in press.
DOI: https://doi.org/10.2138/am-2022-8276. http://www.minsocam.org/

Figure 3

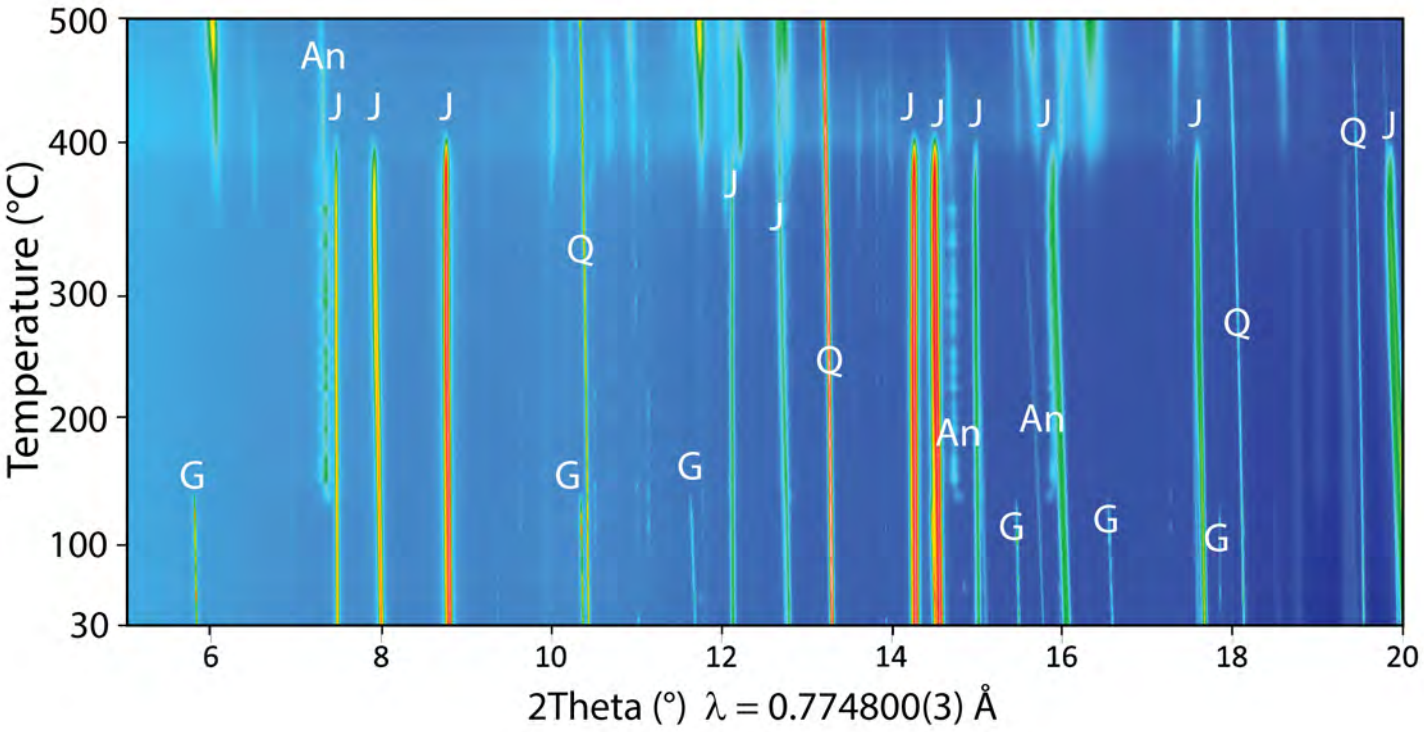

Figure 4

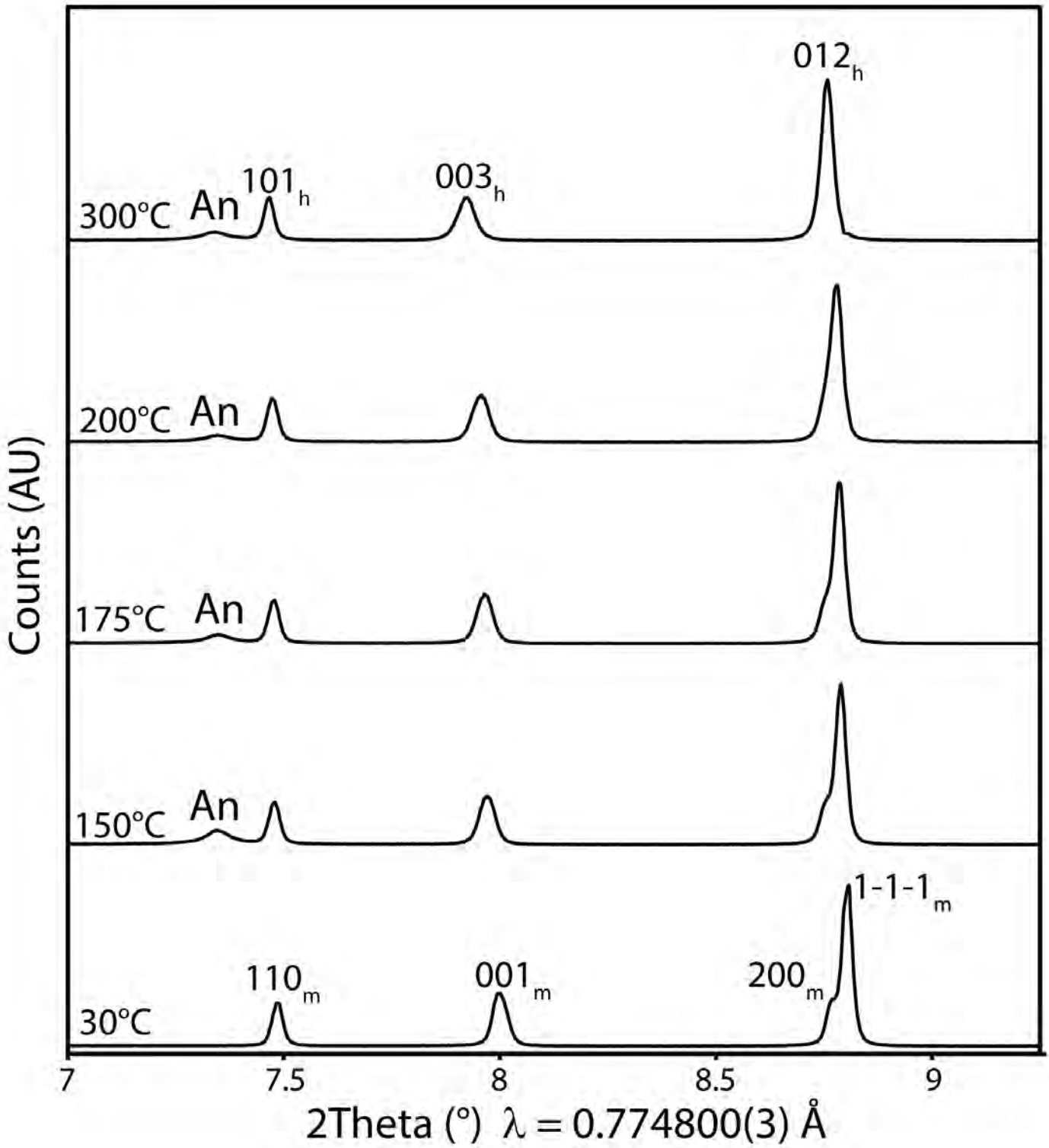

Figure 5

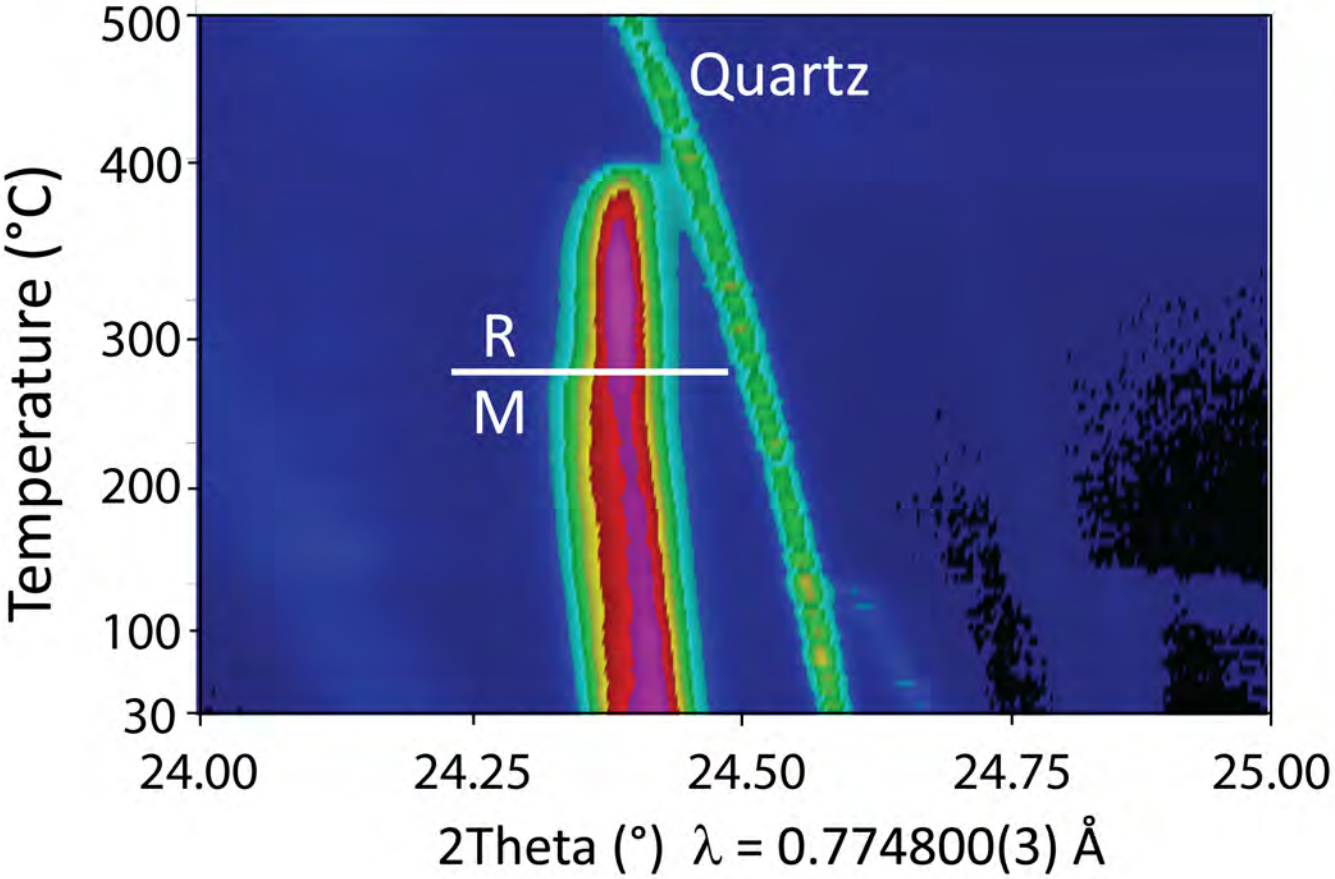

This is the peer-reviewed, final accepted version for American Mineralogist, published by the Mineralogical Society of America.
The published version is subject to change. Cite as Authors (Year) Title. American Mineralogist, in press.
DOI: https://doi.org/10.2138/am-2022-8276. http://www.minsocam.org/

Figure 6

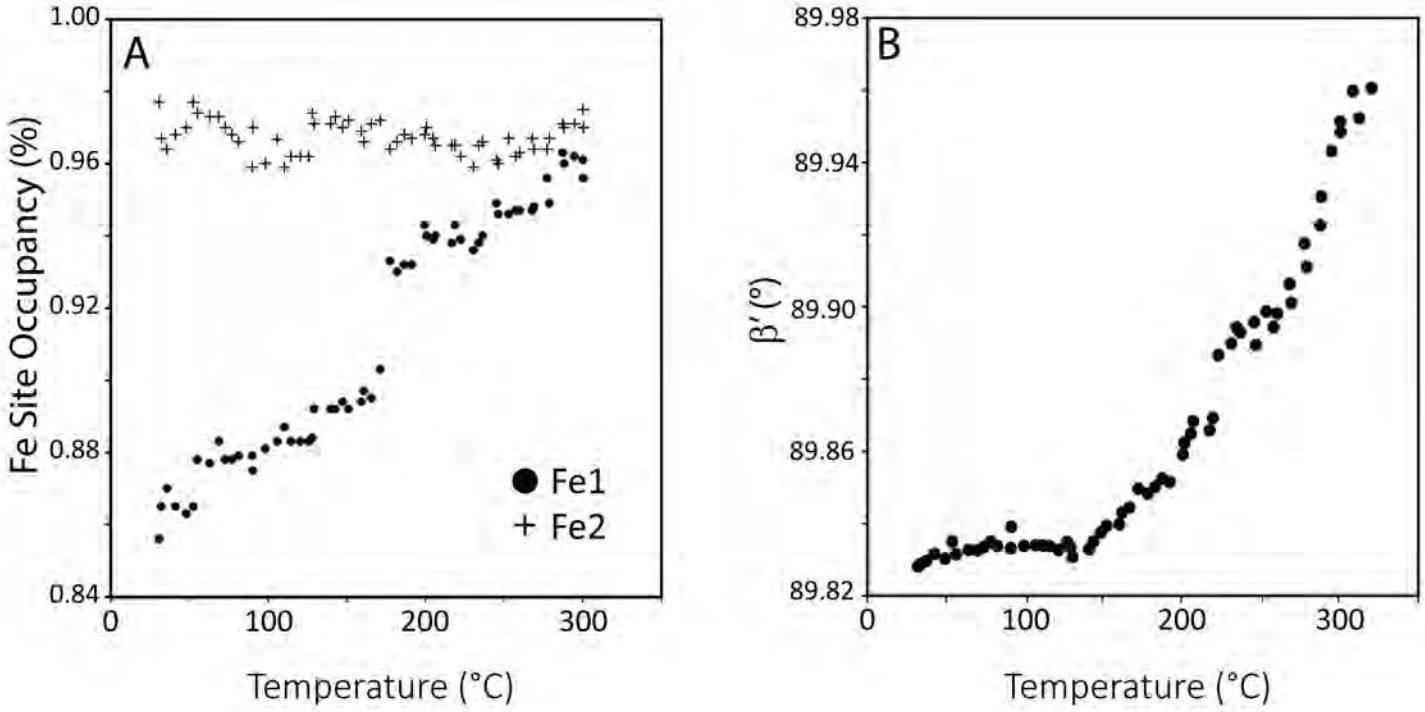

Figure 7

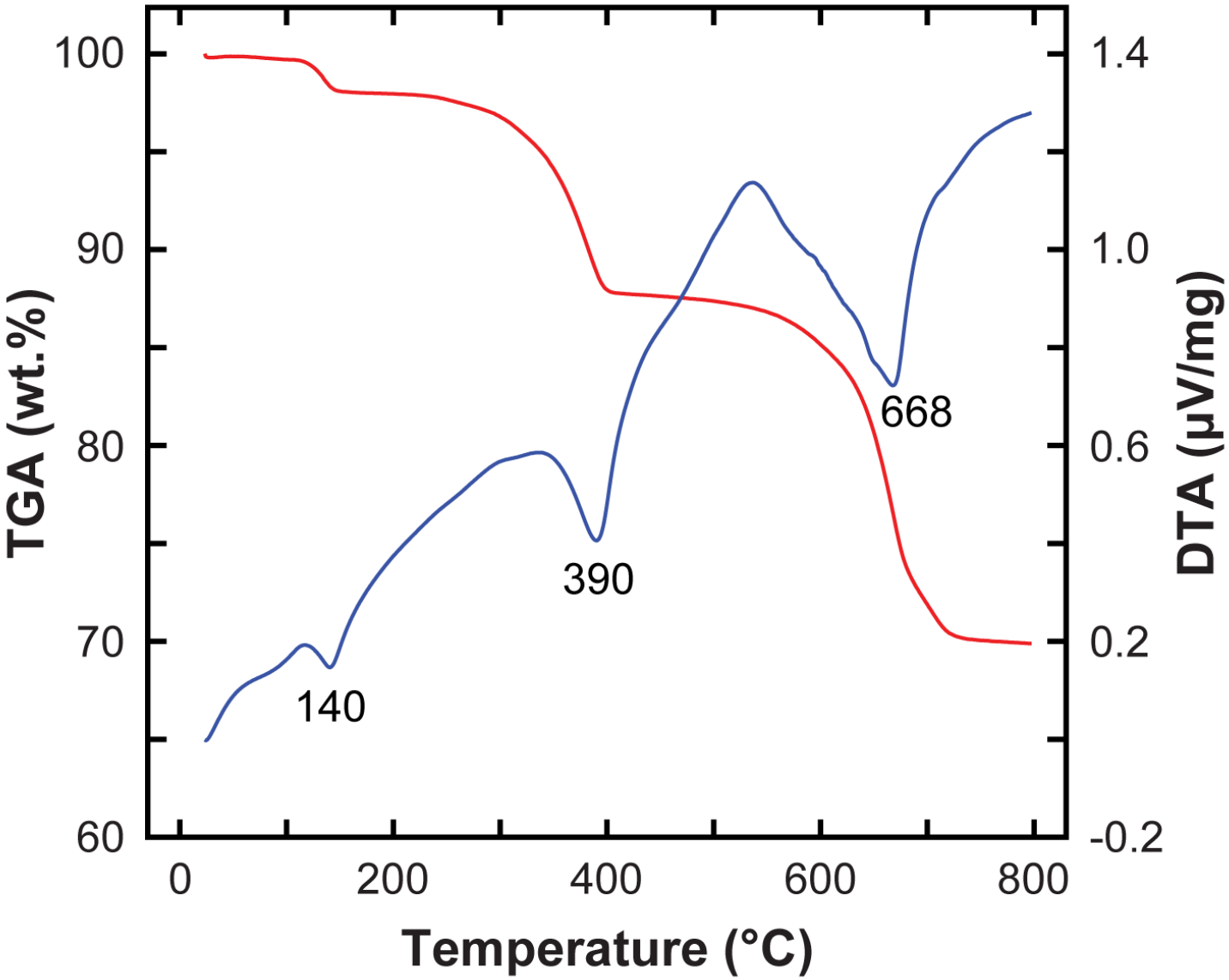

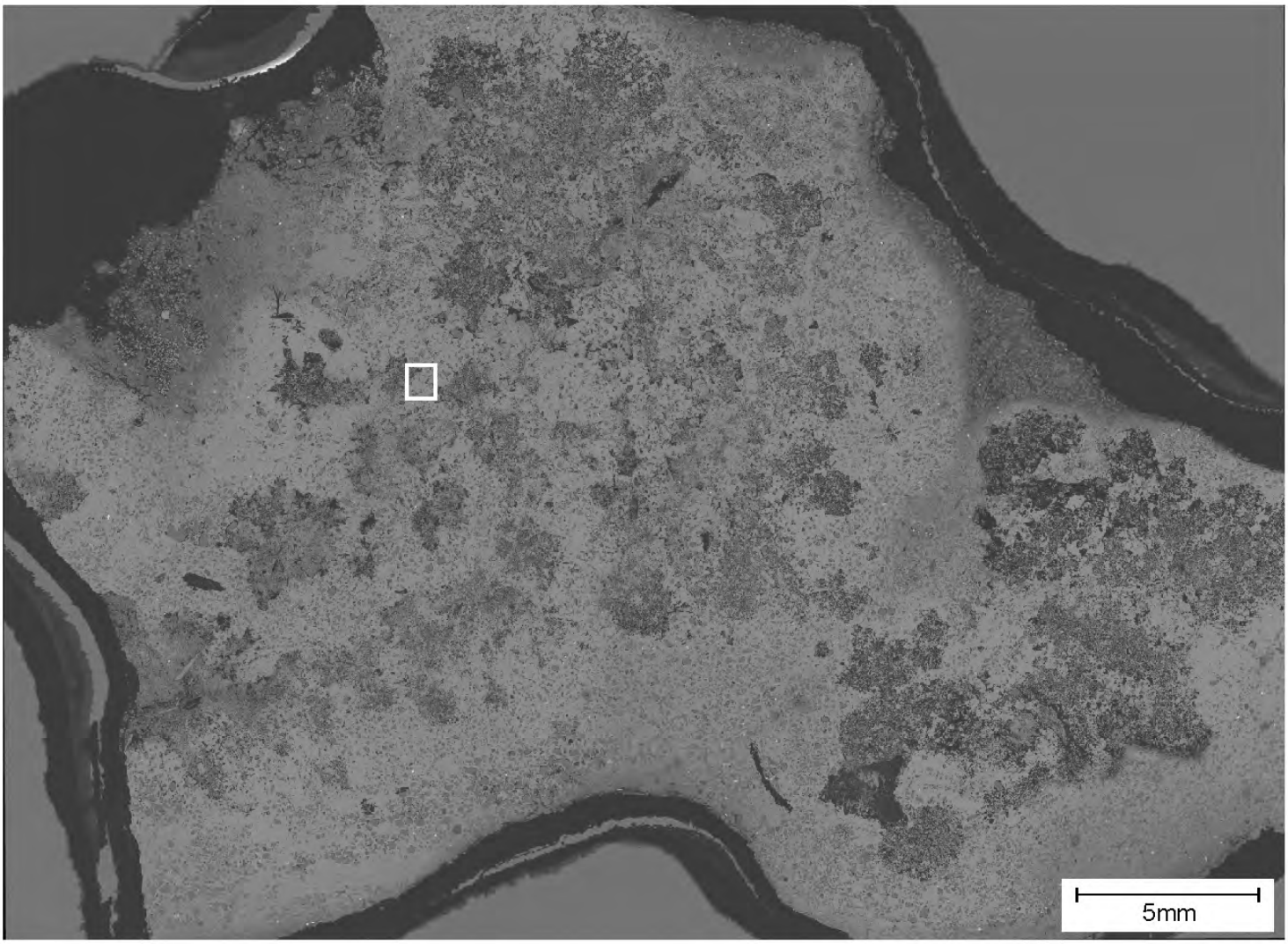

This is the peer-reviewed, final accepted version for American Mineralogist, published by the Mineralogical Society of America.
The published version is subject to change. Cite as Authors (Year) Title. American Mineralogist, in press.
DOI: https://doi.org/10.2138/am-2022-8276. http://www.minsocam.org/

Figure 9

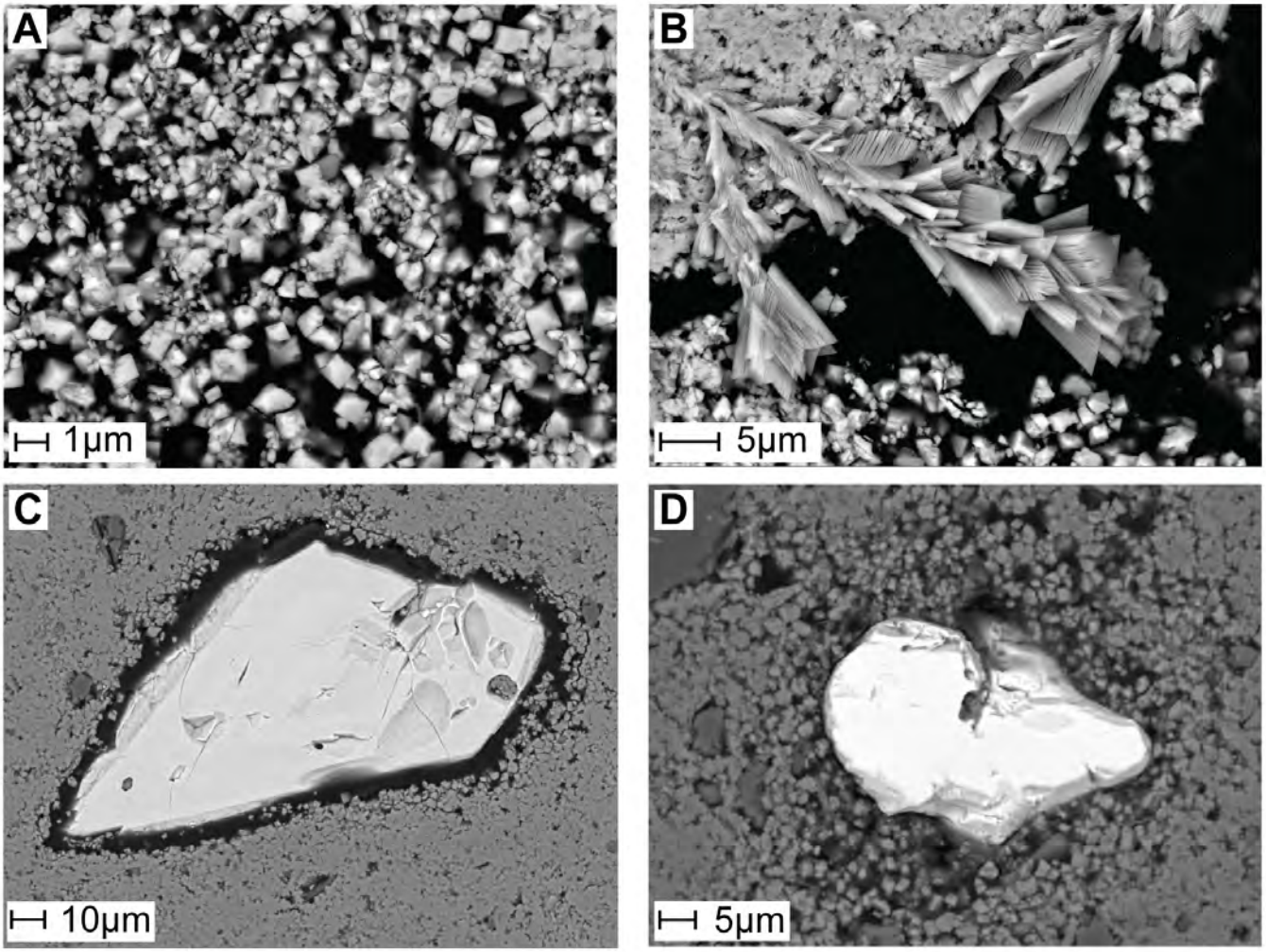

Figure 10